



Anisotropy of upper critical field and surface superconducting state in the intermediate-valence superconductor CeIr₃

Yoshiki J. Sato ^{1,2,*}, Fuminori Honda ², Yusei Shimizu,² Ai Nakamura,² Yoshiya Homma,² Arvind Maurya,² Dexin Li,² Takatsugu Koizumi,^{1,2} and Dai Aoki²

¹Graduate School of Engineering, Tohoku University, Sendai 980-8577, Japan

²Institute for Materials Research, Tohoku University, Oarai, Ibaraki 311-1313, Japan



(Received 7 July 2020; revised 6 October 2020; accepted 19 October 2020; published 10 November 2020)

CeIr₃ is a Ce-based superconductor with a superconducting transition temperature $T_c = 3.4$ K in an intermediate-valence state. We grew high-quality single crystals of CeIr₃ using the Czochralski method, and measured the electrical resistivity, magnetic torque, and specific heat. The anisotropy of the superconducting upper critical field H_{c2} was determined. The temperature dependence of H_{c2} , obtained from the resistivity measurements, suggests the multiband character of the superconductivity in CeIr₃. Different field-angle dependencies of H_{c2} in electrical transport and thermodynamic measurements indicate the robust surface effect in the bulk superconductivity of CeIr₃. We analyzed the surface superconductivity based on simple models to reveal the bulk superconducting properties. Our results support the isotropic bulk superconducting state and robust surface superconductivity in CeIr₃ single crystals.

DOI: [10.1103/PhysRevB.102.174503](https://doi.org/10.1103/PhysRevB.102.174503)

I. INTRODUCTION

Superconductivity in f -electron systems, which have an interplay between superconductivity and magnetic or valence fluctuations, has attracted significant interest both experimentally and theoretically [1–6]. Since the discovery of heavy-fermion superconductivity in the Ce-based compound CeCu₂Si₂ [7], considerable efforts have been made to find unconventional superconductors in Ce-based compounds. Many heavy-fermion superconducting states have been found near the magnetic quantum critical point in Ce compounds, where the magnetic fluctuations are strongly enhanced, playing a role as a glue for superconducting Cooper pairs. Moreover, another important pairing mechanism called valence or charge fluctuation induced superconductivity has been proposed theoretically. The two superconducting domes observed in the temperature-pressure phase diagram of CeCu₂Si₂ and CeCu₂Ge₂ are interpreted by such magnetic and valence fluctuations [8,9]. Although the pairing symmetry was believed to be a nodal d -wave mediated by magnetic fluctuations, several recent experiments support a full-gap superconductivity in CeCu₂Si₂ [10,11]. Furthermore, magnetic and valence fluctuations have been proposed as pairing mechanisms in other f -electron superconductors, such as PuTGe₅ ($T = \text{Co}$ or Rh) [12,13], to explain the relatively high superconducting transition temperature T_c [14–17].

In this study, we focus on a Ce-based intermediate-valence superconductor CeIr₃ with a specific heat coefficient of 25 mJ/(K² mole). CeIr₃ exhibits superconductivity at T_c of 3.4 K [18]. CeIr₃ crystallizes in the PuNi₃-type rhombohedral structure, with the space group $R\bar{3}m$ (No. 166, D_{3d}^5), as shown in Fig. 1(a) [19]. This $R\bar{3}m$ space group is identical

to that of the well-studied semimetal Bi [20], topological insulators Bi₂X₃ ($X = \text{Se}$ or Te) [21,22], and the topological superconductor doped Bi₂Se₃ [23,24]. There are two crystallographically nonequivalent Ce sites (Ce1 and Ce2) in the crystal structure of CeIr₃. The PuNi₃-type structure is described by the stacking of Laves MgCu₂- and CaCu₅-type hexagonal structure blocks [25]. CeIr₃ exhibits nearly temperature-independent paramagnetism at high temperatures, and the Ce ion in CeIr₃ seems to be close to the tetravalent state (Ce⁴⁺) [26]. By analyzing the superconducting transition temperature in La- and Th-doped CeIr₃, the valence number of the Ce atom was estimated to be 3.6 in CeIr₃ [27]. Recently, the strong intermediate-valence character of CeIr₃ has also been reported using x-ray photoelectron spectroscopy [28]. The superconducting properties of CeIr₃ can be explained within the framework of the BCS theory [26,28], but the intermediate-valence state might influence the superconducting properties. From the perspective of the superconductivity and the valence state, it is intriguing to compare the isostructural superconductors CeIr₃, LaIr₃, and ThIr₃. Comparative studies between CeIr₃ and LaIr₃ (or ThIr₃) have been performed using energy band calculations [28–30] and muon spin rotation and relaxation measurements [31,32]. However, the effects of the intermediate-valence state on the superconducting state in CeIr₃ are still unclear. Therefore, studies of the electronic state and superconducting properties using high-quality CeIr₃ single crystals are desired.

In this paper, we report the temperature and field-angle dependence of an upper critical field H_{c2} and an irreversible field H_{irr} using high-quality CeIr₃ single crystals. Little has been reported on the anisotropy of H_{c2} of CeIr₃ because of the difficulty in synthesizing single crystals. Recently, we succeeded in growing single-crystalline CeIr₃ [26,33]. Generally, the temperature and field-angle dependence of H_{c2} are associated with the superconducting properties, such as the

*yoshi.satoh@imr.tohoku.ac.jp

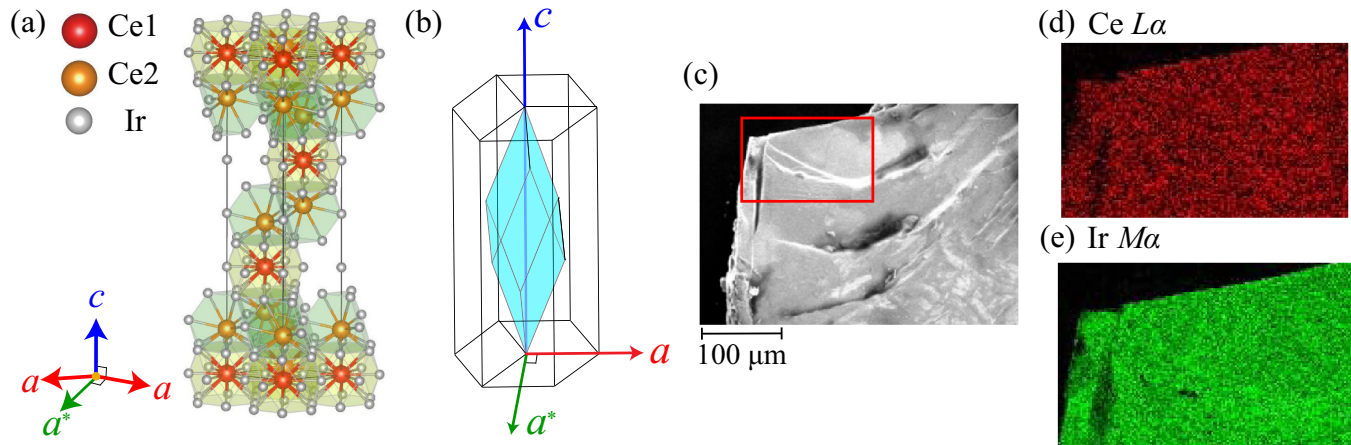


FIG. 1. (a) Crystal structure of CeIr_3 . Ce1, Ce2, and Ir atoms are shown by red, orange, and gray spheres, respectively. (b) Schematic crystal structure expressed by the hexagonal lattice (outer framework) and rhombohedral lattice (blue painted part). (c) SEM image of a CeIr_3 single crystal. The scale bar in the bottom-left corner indicates a length of $100 \mu\text{m}$. EDX elemental mapping of the SEM sample (in the red box) for (d) $\text{Ce } L\alpha$ and (e) $\text{Ir } M\alpha$.

effective mass [34–36], multiband effect [37–39], and Cooper pairing symmetry [40–43]. $H_{c2}(T)$ curves of CeIr_3 are relatively isotropic between $H \parallel a$ and $H \parallel c$, compared with the heavy-fermion superconductors. The $H_{c2}(T)$ curve shows a slightly convex T dependence only for the magnetic field $H \parallel c$, indicating a multiband effect [26]. Interestingly, the angular dependence of the upper critical field $H_{c2}(\theta)$ determined from the electrical resistivity measurements exhibits an unusual cusplike behavior, which has been found to deviate from both the conventional three-dimensional effective mass [Ginzburg-Landau (GL)] model and the two-dimensional Tinkham model [33]. We discuss the cusplike behavior of $H_{c2}(\theta)$ based on a surface superconducting state with a proximity effect in a bulk superconductor. There is very little quantitative data on the surface superconducting state in bulk superconductors. In previous studies, surface superconducting states have been studied for some bulk superconductors such as needlelike whiskers of UPt_3 [44] and MgB_2 powder [45]. We emphasize the importance of a quantitative evaluation of surface superconductivity, which allows us to analyze the bulk superconducting properties.

II. EXPERIMENT

Single crystals of CeIr_3 were prepared using the Czochralski method in a tetra arc furnace in an Ar atmosphere, as reported in our previous study [26]. After synthesis, single crystals were further annealed at 950°C under a 4×10^{-6} Pa vacuum for 6 days. The crystal structure of the single crystals of CeIr_3 in this study was confirmed using a single-crystal x-ray diffractometer (Rigaku XtaLAB mini II) with $\text{Mo } K\alpha$ radiation ($\lambda = 0.71073 \text{ \AA}$). The refined crystal parameters of CeIr_3 are summarized in Tables I and II. The crystal structure was solved with SHELXT, and further refined with SHELXL. CeIr_3 has a rhombohedral structure, and the crystal indices can be defined in two ways: as hexagonal indices with additional translational vectors, or as rhombohedral indices with equal primitive vectors making equal angles with each other. Figure 2(b) shows schematic crystal structures expressed by

the hexagonal lattice (outer framework) and rhombohedral lattice (indicated in blue). In this study, we have selected the conventional way, i.e., hexagonal indices. The a^* axis is perpendicular to the a and c axes.

To confirm the chemical composition and homogeneity of CeIr_3 single crystals, we performed scanning electron microscopy (SEM; JSM-6010LA InTouchScope) and energy-dispersive x-ray spectroscopy (EDX) analyses. As shown in the SEM image in Fig. 1(c), a series of steps and terraces can be observed in consonance with the layered structure on the cleaved surface of the CeIr_3 single crystals. We analyzed the spectra of $\text{Ce-}L\alpha$ (4.839 keV) and $\text{Ir-}M\alpha$ (1.977 keV), and obtained the EDX elemental mapping, as shown in Figs. 1(d) and 1(e). The EDX results indicate that Ce and Ir are distributed uniformly, and the composition of Ce:Ir is 1:3 in the CeIr_3 single crystals.

The single crystals were oriented using a Laue camera (Photonic Science Laue x-ray CCD camera) and cut using a spark cutter. The typical dimensions of the samples in the electrical transport measurements are $1 \text{ mm} \times 0.2 \text{ mm} \times 0.2 \text{ mm}$

TABLE I. Crystallographic and structure refinement data of CeIr_3 .

Parameter	Value
Empirical formula	CeIr_3
Formula weight	716.78
Crystal system	Rhombohedral
Space group	$R\bar{3}m$ (No. 166)
a (\AA)	5.2842(6)
c (\AA)	26.216(5)
Volume (\AA^3)	633.95(16)
Formula units per cell (Z)	9
Measured reflections	311
Goodness of fit	1.062
$R1$ [$I > 2.00\sigma(I)$]	0.0414
R (all reflections)	0.0457
$wR2$ (all reflections)	0.1050
Maximum shift/error	0.000

TABLE II. Atomic positions and equivalent isotropic displacement parameters of CeIr₃.

Atom	Site	x	y	z	B_{eq}
Ce1	3a	0	0	0	0.42(4)
Ce2	6c	0	0	0.13934	0.30(3)
Ir1	3b	0	0	1/2	0.27(3)
Ir2	18h	0.50073	0.49928	0.08249	0.19(2)
Ir3	6c	0	0	0.33333	0.56(3)

[see the photograph in Fig. 2(a)]. The electrical resistivity was measured by a four-probe AC method using a Quantum Design physical property measurement system (PPMS) with a rotator probe at temperatures ranging from 1.7 to 300 K. At lower temperatures in the range of 0.03 to 1.2 K, the resistivity was measured by a four-probe DC method using a rotator probe in a dilution refrigerator. Magnetic torque measurements were performed using a membrane-type surface stress sensor (MSS) in accordance with a method proposed in a previous study [46]. A photograph of the mounted crystal is shown in Fig. 4. The magnetic torque signal was detected in a Wheatstone bridge circuit, using a lock-in amplifier with a frequency of 79.3 Hz. The sample was cooled to 1.7 K in the PPMS, with a rotator for the magnetic torque measurements. The specific heat was measured by a relaxation method at the various field angles using a laboratory-made specific heat sample puck holder in the PPMS.

III. RESULTS

Figure 2(a) shows the temperature dependence of the electrical resistivity $\rho(T)$ for currents $J \parallel a$ and $J \parallel c$. $\rho(T)$ exhibits a slightly concave downward curvature in both current directions at approximately 100 K and a clear superconducting transition at $T_c = 3.4$ K. T_c is defined as the midpoint of the resistivity drop, i.e., $\rho(T_c) = 0.5\rho_{n0}$, where ρ_{n0} is the residual resistivity of the normal state. $\rho(T)$ follows T -squared dependence below 8 K, and the residual resistivity ratio $\rho(300 \text{ K})/\rho_{n0}$ of CeIr₃ crystals in this study is about 2. The isotropic resistivity is consistent with the isotropic temperature dependence of the magnetic susceptibility, as reported in a previous work [26]. The PuNi₃-type structure is described as a layered structure with stacking of MgCu₂- and CaCu₅-type structure blocks [25]. However, the electronic state in CeIr₃ appears to be three-dimensional, as seen in the resistivity data.

Figure 2(b) shows the temperature dependence of H_{c2} for the magnetic fields $H \parallel a$ and $H \parallel c$. The estimated upper critical fields $H_{c2}^{\parallel}(0)$ ($H \parallel a$) and $H_{c2}^{\perp}(0)$ ($H \parallel c$) are 6.45 and 4.65 T, respectively. The anisotropic parameter $\Gamma \equiv H_{c2}^{\parallel}/H_{c2}^{\perp}$ is about 1.4 at the lowest temperature, indicating the rather isotropic superconducting state in CeIr₃; however, the initial slopes $|-dH_{c2}^{\parallel}/dT|_{T=T_c} = 4.18 \text{ T/K}$ and $|-dH_{c2}^{\perp}/dT|_{T=T_c} = 0.96 \text{ T/K}$ are very anisotropic, as shown in the inset of Fig. 2(b). The $H_{c2}(T)$ curve is convex in the low magnetic field range for $H \parallel c$, suggesting a multiband effect in the superconductivity of CeIr₃. In contrast, the H_{c2} curve is slightly concave downward for $H \parallel a$. As will be

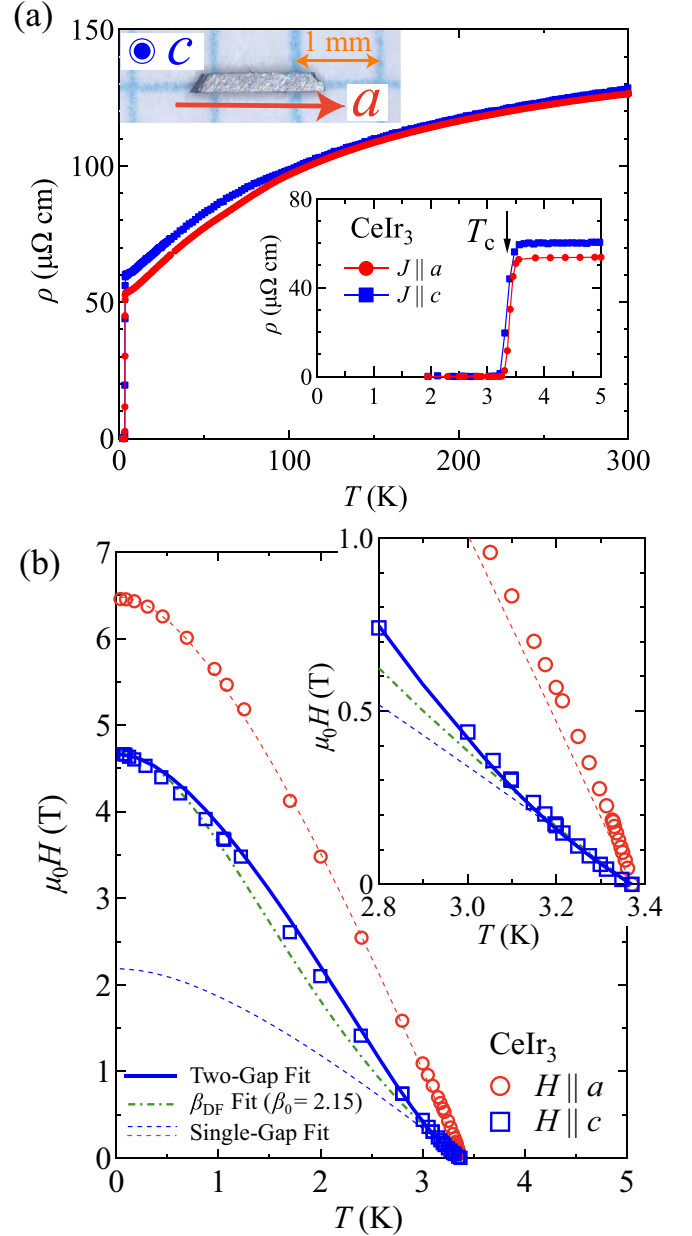


FIG. 2. (a) Temperature dependence of electrical resistivity ρ for the electrical current $J \parallel a$ and $J \parallel c$. The inset shows an enlarged $\rho(T)$ below 5 K. The photograph in the main panel is one of the measured single crystals of CeIr₃. (b) Temperature dependence of the upper critical field H_{c2} for the magnetic field $H \parallel a$ (red circles) and $H \parallel c$ (blue squares). The solid and dashed lines show the two-gap and single-gap models, respectively. The dashed-dotted line shows the scaled Werthamer-Helfand-Hohenberg-Maki (WHHM) model, with $\beta_0 = 2.15$. The inset shows an enlarged view of H_{c2} vs T in the low-field region.

discussed later, the contrasting temperature dependence of H_{c2} between $H \parallel a$ and $H \parallel c$ may be associated with the surface superconducting state of CeIr₃ single crystals. We estimated the coherence lengths as $\xi_{ab}(0) = \sqrt{\phi_0/[2\pi H_{c2}^{\perp}(0)]} = 84 \text{ \AA}$ and $\xi_c(0) = \phi_0/2\pi H_{c2}^{\parallel}(0)\xi_{ab}(0) = 61 \text{ \AA}$, where ϕ_0 is the magnetic flux quantum. Assuming a spherical Fermi surface, the mean-free path l is estimated to be $1.533 \times 10^6/(\rho_{n0}S_s) =$

60 Å for $T \rightarrow 0$ [35]. Here, the cross section of Fermi surface S_s is calculated to be $3.71 \times 10^{20} \text{ m}^{-2}$, using the average of the experimental initial slope. l is close to $\xi_{ab}(0)$ and $\xi_c(0)$, and these parameters obtained in this study are intermediate values between the dirty and clean limits.

To further analyze the H_{c2} curve of CeIr₃, we calculated H_{c2} . The experimental $H_{c2}(T)$ curve for $H \parallel c$ deviates from the single-gap model for the dirty limit [47], as shown in Fig. 2. To explain the convex $H_{c2}(T)$ curve, we calculated $H_{c2}(T)$ for two-gap superconductivity. For a multiband system with interband coupling constants ($\lambda_{12}, \lambda_{21}$) and intraband coupling constants ($\lambda_{11}, \lambda_{22}$), the equations for $H_{c2}(T)$ are as follows [37,48]:

$$a_0[\ln t + U(h)][\ln t + U(\eta h)] + a_2[\ln t + U(\eta h)] + a_1[\ln t + U(h)] = 0, \quad (1)$$

$$U(h) = \psi\left(\frac{1}{2} + h\right) - \psi\left(\frac{1}{2}\right), \quad (2)$$

where $a_0 = 2(\lambda_{11}\lambda_{22} - \lambda_{12}\lambda_{21})/[(\lambda_{11} - \lambda_{22})^2 + 4\lambda_{12}\lambda_{21}]$, $a_1 = 1 + (\lambda_{11} - \lambda_{22})/[(\lambda_{11} - \lambda_{22})^2 + 4\lambda_{12}\lambda_{21}]$, $a_2 = 1 - (\lambda_{11} - \lambda_{22})/[(\lambda_{11} - \lambda_{22})^2 + 4\lambda_{12}\lambda_{21}]$, $h = H_{c2}D_1/(2\phi_0 T)$, $t = T/T_c$, and $\psi(x)$ is the digamma function. η is the ratio of the diffusivities of bands D_1 and D_2 , and the obtained value of D_2/D_1 is 23, indicating the different contributions from two-dimensional and three-dimensional Fermi surfaces. As shown in Fig. 2(b), we obtained a good fit across the entire temperature range with the fitting parameters $\lambda_{11} = 0.850$, $\lambda_{22} = 0.331$, $\lambda_{12} = 0.257$, $\lambda_{21} = 0.105$. The energy band calculations of CeIr₃ with the electron-electron interactions U and spin-orbit coupling effect have been reported in a previous study [28]. The energy band calculations revealed multiple bands crossing the Fermi energy, in which the Fermi surfaces consist of pocket Fermi surfaces near the Γ point in the Brillouin zone and a large cylindrical Fermi surface with complicated arm structures. The multiband behavior in $H_{c2}^\perp(T)$ may be consistent with the calculated two-dimensional and three-dimensional Fermi surfaces.

As another scenario to explain the convex $H_{c2}(T)$ curve, we calculated the modified single-gap model [49], using the following equation:

$$H_{c2}(T) = \beta(T)H_{c2}^{\text{WHHM}}(T) = \frac{\beta_0 H_{c2}^{\text{WHHM}}(T)}{1 + (\beta_0 - 1)T^2/T_{c0}^2}, \quad (3)$$

where T_{c0} is the superconducting transition temperature in a zero field, and β_0 is a fitting parameter. $H_{c2}^{\text{WHHM}}(T)$ is the H_{c2} curve of a dirty-limit single-gap superconductor. $\beta(T)$ is an empirical function that includes the effect of strong coupling and anisotropy. The fitting result of the modified single-gap model shows a convex curve with a fitting parameter of $\beta_0 = 2.15$, as shown by the green dashed-dotted line in Fig. 2(b). However, the fitting result of the two-gap model is in better agreement with the experimental $H_{c2}(T)$ curve over a wide temperature range.

Figure 3(a) shows the temperature dependence of the resistivity at different field angles for $J \parallel a$ at $T = 1.7 \text{ K}$ ($0.5T_c$). The superconducting transition remains sharp under the magnetic fields, enabling an accurate determination of H_{c2} as a function of the magnetic field angle θ . Interestingly, the angular dependence of $H_{c2}(\theta)$ determined using the criterion

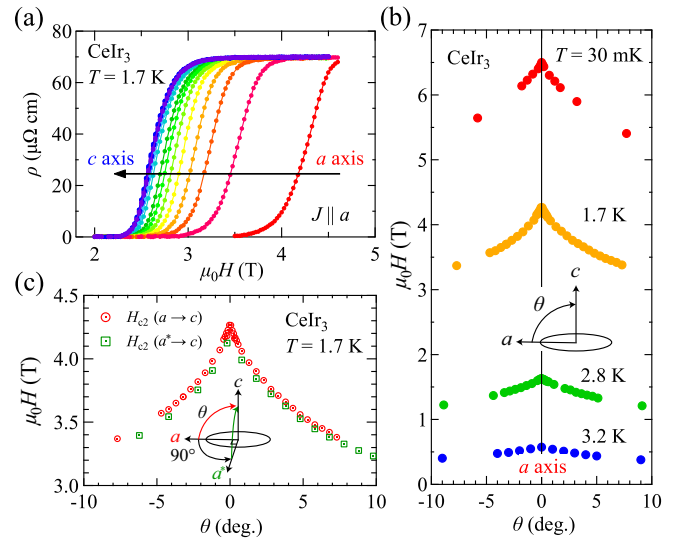


FIG. 3. (a) Temperature dependence of electrical resistivity $\rho(T)$ at different field angle from $\theta = 0^\circ$ ($H \parallel a$) to 90° ($H \parallel c$) every 5° step for $J \parallel a$ at $T = 1.7 \text{ K}$ ($0.5T_c$). (b) Angular dependence of the upper critical field $H_{c2}(\theta)$ obtained from electrical resistivity measurements at $T = 0.03, 1.7, 2.8,$ and 3.2 K . (c) $H_{c2}(\theta)$ determined from electrical resistivity measurements for $H \parallel a \rightarrow c$ and $H \parallel a^* \rightarrow c$ at $T = 1.7 \text{ K}$.

of $\rho = 0.5\rho_{n0}$ exhibits cusplike behavior at $\theta = 0^\circ$ (in the ab plane), as shown in Figs. 3(b) and 3(c). $H_{c2}(\theta)$ exhibits cusplike behavior regardless of the definition of H_{c2} , such as $\rho = 0.9\rho_{n0}$ and $\rho = 0.1\rho_{n0}$. The characteristic cusplike behavior is observed in all temperature ranges below T_c , as shown in Fig. 3(b). Figure 3(c) shows $H_{c2}(\theta)$ for $H \parallel a \rightarrow c$ and $H \parallel a^* \rightarrow c$, and the in-plane angular dependence of the upper critical field $H_{c2}(\varphi)$ shows no distinct change.

We also performed magnetic torque measurements to determine a characteristic field for comparison with H_{c2} obtained from the electrical resistivity measurements. Plate-shaped single-crystalline samples were used for magnetic torque measurements. The cusplike behavior in $H_{c2}(\theta)$ was confirmed by electrical resistivity measurements in the same sample. The magnetic torque $\tau/V = \mathbf{M} \times \mathbf{B} \sim \mathbf{M} \times \mathbf{H}$, where V and \mathbf{M} are the volume and magnetization of the sample, was measured using the MSS probe as a function of the magnetic field at fixed angles and temperatures, as shown in Fig. 4. The clear hysteresis resulting from the flux-pinning effect of a type-II superconductor is observed in the field dependence of the magnetic torque τ at each field angle, and the bulk superconductivity in CeIr₃ was confirmed, as reported from magnetization and heat capacity measurements in a previous study [26]. As shown in the inset of Fig. 4, τ shows a clear peak effect, and it is observed in several superconductors, such as cuprate superconductors [50] and some heavy-fermion superconductors [51]. We define the following characteristic fields: the maximum of the peak for the field increasing (H_{max}) and decreasing ($*H_{\text{max}}$) branch of the hysteresis loop, and the onset of the peak: H_{on} (increasing) and $*H_{\text{on}}$ (decreasing). The separation of the two onset fields (H_{on} and $*H_{\text{on}}$) is larger than the separation of the maximum fields (H_{max} and $*H_{\text{max}}$), resembling the magnetic torque

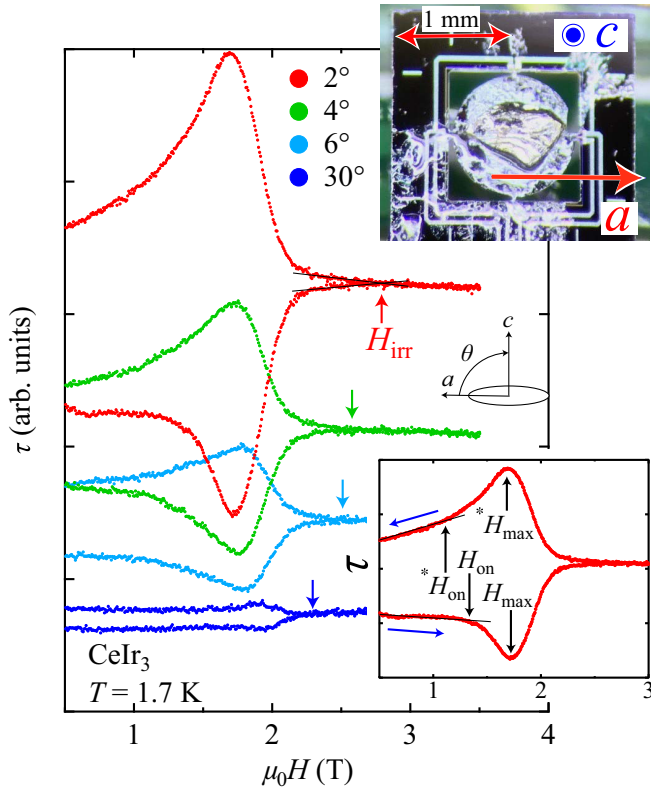


FIG. 4. Field dependence of magnetic torque τ measured at $T = 1.7$ K and magnetic field angle $\theta = 2^\circ, 4^\circ, 6^\circ,$ and 30° for clarity. The magnetic torque data are shifted vertically for $\theta = 4^\circ, 6^\circ,$ and 30° . The irreversibility field H_{irr} is indicated by arrows. The inset shows a zoom of τ vs $\mu_0 H$ at $\theta = 2^\circ$. Various characteristic fields are indicated by arrows in the inset: $H_{\text{on}}, {}^*H_{\text{on}}, H_{\text{max}},$ and ${}^*H_{\text{max}}$ (see text for details). The direction of the field sweep is indicated by blue arrows. The photograph in the main panel is a sample mounted on an MSS probe.

behavior of CeRu_2 [52] and $2H\text{-NbSe}_2$ [53], in which the peak effect occurs because of the two distinct vortex-matter phases, namely the order-disorder phase transition [54]. We can define an irreversible field H_{irr} , where the two branches of the hysteresis loops meet. In type-II superconductors, H_{c2} corresponds to the phase transition from superconducting to normal state, while H_{irr} gives the magnetic field at which the superconducting vortex starts melting or moving. Some parts of H_{irr} are influenced by surface [55] or geometrical barriers [56]; however, H_{irr} provides information about the bulk superconducting properties.

To obtain more information on the bulk superconducting transition of CeIr_3 , we measured the field dependence of the specific heat at $T = 1.85$ K at various magnetic field angles θ , as shown in Fig. 5(a). $C(H)/T$ shows a clear superconducting transition at approximately $\mu_0 H \approx 2$ T at $T = 1.85$ K. The upper critical field H_{c2} obtained from the specific heat measurements is smaller than H_{c2} obtained from the electrical resistivity measurements using the same criteria, as reported in previous studies [26,28]. Here H_{c2} is determined by the midpoint estimated using two linear extrapolation lines, as shown in the data for $\theta = 10^\circ$ of Fig. 5(a). Figure 5(b) shows the angular dependence of bulk H_{c2} obtained from the

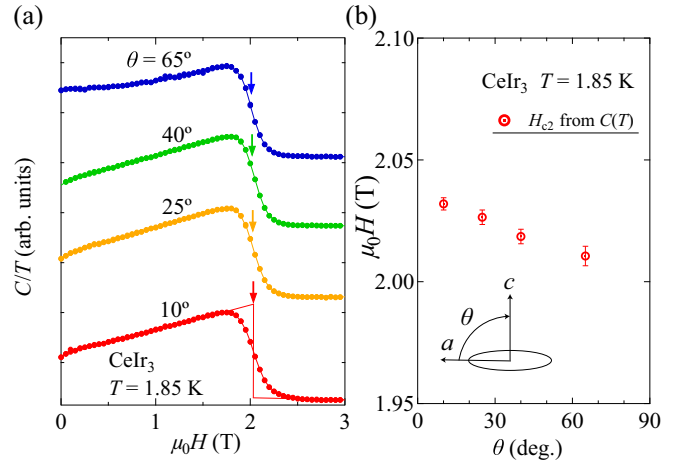


FIG. 5. (a) Field dependence of specific heat in the form of C/T measured at $T = 1.85$ K at the various field angles. The measured field angles are $\theta = 10^\circ, 25^\circ, 40^\circ,$ and 65° . The upper critical field H_{c2} is determined by the midpoint estimated using two linear extrapolation lines, as shown in the data of $\theta = 10^\circ$. The determined H_{c2} is indicated by arrows. (b) Angular dependence of H_{c2} (red circles) obtained from the specific heat measurements at $T = 1.85$ K.

specific heat measurements at 1.85 K. In contrast to the $H_{c2}(\theta)$ obtained from the electrical resistivity measurements, the cusplike behavior is not seen in $H_{c2}(\theta)$ obtained from the specific heat measurements.

IV. DISCUSSION

Figure 6(a) shows the field-angle dependence of H_{c2} obtained from the electrical resistivity measurements at $T = 1.7$ K ($\approx 0.5T_c$). $H_{c2}(\theta)$ exhibits cusplike behavior at $\theta = 0^\circ$ ($H \parallel a$). In order to elucidate the origin of the characteristic angular dependence of H_{c2} , it is useful to compare the experimental $H_{c2}(\theta)$ with conventional models that describe $H_{c2}(\theta)$, i.e., the GL model and the two-dimensional Tinkham model.

According to the GL model [34], the angular dependence of H_{c2} can be described by the following equation:

$$\left(\frac{H_{c2}(T, \theta) \sin \theta}{H_{c2}^\perp(T)}\right)^2 + \left(\frac{H_{c2}(T, \theta) \cos \theta}{H_{c2}^\parallel(T)}\right)^2 = 1. \quad (4)$$

The calculated results are shown as blue dashed lines in Fig. 6(a). The experimental H_{c2} data deviated largely from the GL model, and the cusplike behavior could not be reproduced by the GL model.

In two-dimensional superconductors such as superconducting thin films [57] and superlattices [58], the angular dependence of H_{c2} obeys the following equation, first derived by Tinkham [59]:

$$\left|\frac{H_{c2}(T, \theta) \sin \theta}{H_{c2}^\perp(T)}\right| + \left(\frac{H_{c2}(T, \theta) \cos \theta}{H_{c2}^\parallel(T)}\right)^2 = 1. \quad (5)$$

The Tinkham model shows the cusplike feature, as shown by the green dash-dotted lines in Fig. 6(a), but the experimental

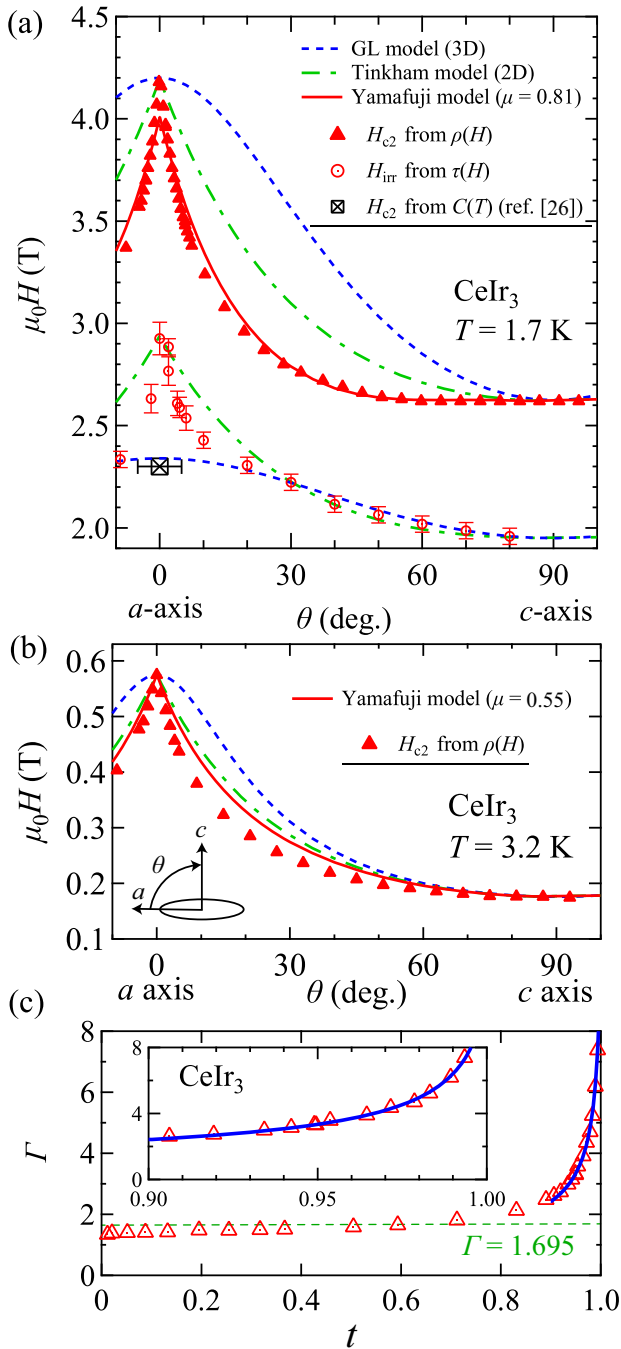


FIG. 6. (a) Angular dependence of H_{c2} (red triangles) obtained from electrical resistivity measurements and H_{irr} (red open circles) obtained from magnetic torque measurements at $T = 1.7$ K ($\approx 0.5T_c$). Bulk H_{c2} estimated from specific heat measurements in Ref. [26] is indicated by a black square. Dashed (blue) and dashed-dotted (green) lines represent the fitting results using Eq. (4) and Eq. (5), respectively. The solid red line is the fitting curve using Eq. (6) with a proximity effect (see the text). (b) Angular dependence of H_{c2} (red triangles) obtained from electrical resistivity measurements at $T = 3.2$ K ($\approx 0.95T_c$). (c) The anisotropic parameter $\Gamma \equiv H_{c2}^{\parallel}/H_{c2}^{\perp}$ as a function of the renormalized temperature $t = T/T_c$ extracted from electrical resistivity measurements. The inset shows the enlarged Γ vs t between $t = 0.9$ and 1.0 . The solid blue line is the fitting curve using Eq. (7).

H_{c2} data deviate from the Tinkham model. The experimental $H_{c2}(\theta)$ shows a steeper curvature than that in the Tinkham model.

We analyzed $H_{c2}(\theta)$ based on a surface superconducting state, namely the third critical field H_{c3} [60]. Yamafuji *et al.* proposed the following approximate formula for isotropic superconductors [61]:

$$\left(\frac{H_{c3}(T, \theta)}{H_{c2}^{\perp}(T)/\mu^2} \cos \theta\right)^2 [1 + \tan \theta (1 - \sin \theta)] + \left(\frac{H_{c3}(T, \theta)}{H_{c2}^{\perp}(T)} \sin \theta\right) = 1, \quad (6)$$

where μ is a coefficient obtained from the numerical analysis, and $1/\mu^2$ corresponds to the anisotropy of the $H_{c3}(\theta)$. Here, we considered the experimental $H_{c2}(T, \theta)$ obtained from the electrical resistivity measurements as the third critical field $H_{c3}(T, \theta)$, and assumed the isotropic bulk upper critical field [$= H_{c2}^{\perp}(T)$]. The solid red line in Fig. 6(a) shows the best fit for the experimental data obtained using Eq. (6) by varying the parameter μ . The experimental $H_{c2}(\theta)$ is well described by the Yamafuji model, including the characteristic flat angular dependence around $H \parallel c$.

Figure 6(b) shows the field-angle dependence of H_{c2} at $T = 3.2$ K ($\approx 0.95T_c$) obtained from the electrical resistivity measurements. The experimental $H_{c2}(\theta)$ becomes close to that in the simple Tinkham model. This is presumably because of the fact that the superconducting coherence length $\xi \propto (T_c - T)^{-1/2}$ diverges near the superconducting critical temperature $T_c = 3.4$ K, and becomes much longer than the characteristic length of the surface superconductivity.

Figure 6(a) also shows the field-angle dependence of H_{irr} obtained from the magnetic torque measurements at $T = 1.7$ K. $H_{irr}(\theta)$ exhibits a cusplike behavior at $\theta = 0^\circ$; however, no flat behavior of $H_{irr}(\theta)$ was seen around $H \parallel c$. The irreversible field H_{irr} deviates from that in the GL model. We also show the bulk H_{c2}^{\parallel} estimated from specific heat measurements in a previous study [26], and find that the bulk H_{c2}^{\parallel} is smaller than H_{irr} for $H \parallel a$, indicating the surface effects.

Figure 6(c) shows the anisotropic parameter $\Gamma(t) \equiv H_{c2}^{\parallel}(t)/H_{c2}^{\perp}(t)$ as a function of the renormalized temperature $t = T/T_c$. $\Gamma(t)$ is extracted from the electrical resistivity measurements. At low temperatures, Γ has a constant value. By contrast, Γ starts to diverge above $t = 0.8$ and reaches $\Gamma \sim 8$ at just below $t = 1.0$. Such divergent behavior of the anisotropy parameter $\Gamma(t)$ has been reported in superconductivity of thin films [62] and superlattices [63]. The divergent behavior of the anisotropic parameter $\Gamma(t)$ may be explained by surface effects. We assume an extremely thin film of an isotropic superconductor to explain the temperature dependence of Γ . The upper critical field perpendicular to the thin film is described as $H_{c2}^{\perp}(T) = \phi_0/[2\pi\xi^2(T)] \propto (T_c - T)$ based on the Ginzburg-Landau theory. On the other hand, the critical field parallel to the thin film is given by $H_{c2}^{\parallel}(T) = 2\sqrt{6}H_c(T)\lambda(T)/d \propto (T_c - T)^{1/2}$ [59]. Here, H_c is the thermodynamic critical field, and d is the thickness of the film. From these expressions, we obtain the temperature

dependence of Γ as

$$\Gamma(T) \equiv \frac{H_{c2}^{\parallel}(T)}{H_{c2}^{\perp}(T)} \propto \frac{(T_c - T)^{\frac{1}{2}}}{(T_c - T)} = (T_c - T)^{-\frac{1}{2}}. \quad (7)$$

Equation (7) is valid near the transition temperature, and is based on the simplified model without the anisotropy of the effective mass and multiband effect. However, the experimental $\Gamma(t)$ is qualitatively well described near T_c by $\Gamma = a(T_c - T)^{-\frac{1}{2}}$, where a is a fitting parameter, as shown in Fig. 6(c). Taking the characteristic field-angle dependence of H_{c2} and the divergent behavior of $\Gamma(t)$ into account, the anisotropy of H_{c2} in CeIr₃ single crystals is attributed to the surface superconducting state. The important consideration here is the value of the anisotropy parameter. The superconducting regions can nucleate at a metal-vacuum interface in a parallel magnetic field H_{c3} , which is higher than H_{c2} by a factor of 1.695 in an isotropic material [60]. The experimental anisotropy $H_{c3}(0^\circ)/H_{c3}(90^\circ) \sim H_{c3}(0^\circ)/H_{c2}(90^\circ)$ is smaller than 1.695, at temperatures lower than $0.5T_c$. Considering the anisotropic effective mass and the temperature dependence of the critical field ratio H_{c3}/H_{c2} [64,65], the experimental anisotropy should be larger than 1.695, as is the case in UPt₃ [66]. We attribute this small anisotropy to the proximity effect when the superconducting wave function extends from the surface superconducting layer into the interface in the magnetic field of $H_{c3} > H > H_{c2}$ [62,67]. The proximity effect is dominant only in the low-temperature region below $0.5T_c$.

The cusplike behavior is absent in the $H_{c2}(\theta)$ determined from the specific heat measurements, and the bulk upper critical field is isotropic in CeIr₃, as shown in Fig. 5(b). The small difference between the experimental H_{c2} determined from the electrical resistivity measurements and theoretical H_{c3} for isotropic superconductors [see Figs. 6(a) and 6(b)] also suggests the isotropic bulk H_{c2} of CeIr₃. A comparison of CeIr₃ with other superconductors that crystallize in the $R\bar{3}m$ space group may be interesting from the viewpoint of the anisotropic superconducting state. In this crystal structure, the a^*-c plane is a mirror-symmetry plane, whereas the $a-c$ plane is not. The existence (or absence) of the mirror symmetry is related to the anisotropic superconducting state in doped Bi₂Se₃ [68]. Consequently, Cu_xBi₂Se₃ [24] and Sr_{0.1}Bi₂Se₃ [69] exhibit a clear in-plane anisotropy of the superconducting properties. Precise investigations of the in-plane anisotropy of the superconducting state by thermodynamic measurements, which are not affected by the surface effect, may be interesting for future studies.

The presence of impurity phases causing the discrepancy between the upper critical fields determined from electrical transport and thermodynamic measurements may be possible. Some superconductors containing Ce and Ir have been reported: CeIr₂ ($T_c = 0.21$ K) [70,71], CeIr₅ ($T_c = 1.82$ K) [18], and Ir ($T_c = 0.14$ K) [72]. To the best of our knowledge, T_c of CeIr₃ is the highest value among Ce-Ir binary compounds and elemental superconductors. The EDX results [Figs. 1(d) and 1(e)] also indicate that the reported superconducting properties in the present work are inherent in CeIr₃.

Generally, the surface superconducting state is sensitive to boundary conditions. For UPt₃, whiskers-like crystals grown by rapid cooling and needlelike crystals grown by

a bismuth-flux method exhibit surface superconductivity [44,66]. However, the surface effects in whiskers-like and needlelike crystals have not been observed in the Czochralski-grown single crystals, which were cut using a spark cutter, as in the present study [44]. Therefore, the robust surface superconductivity in CeIr₃ is rather surprising. Other single crystal growth techniques may be helpful in obtaining single-crystalline CeIr₃ without surface effects, but the high melting point (~ 2000 °C) and the incongruent melting property [73] of CeIr₃ make it difficult to grow single crystals using other techniques. We emphasize that the evaluation of surface superconductivity allows the analysis of the bulk superconducting properties.

It would be intriguing to examine the anisotropy of H_{c2} in LaIr₃ and ThIr₃ to study the effect of intermediate-valence character in the bulk superconducting state of CeIr₃. Our results may help to better understand the superconducting state in intermediate-valence Ce compounds and the valence fluctuation mediated superconductivity.

V. CONCLUSIONS

In this study, the anisotropy of the upper critical field H_{c2} for CeIr₃, which shows a superconducting transition at $T_c = 3.4$ K in the intermediate-valence state, was precisely examined using successfully grown high-quality single crystals. The temperature dependence of H_{c2} obtained from resistivity measurements suggests the multiband character of the superconductivity in CeIr₃. More detailed experimental and theoretical studies are necessary to reveal the details of the multiband superconducting property. A remarkable angular dependence of $H_{c2}(\theta)$ was observed in the resistivity measurements, while such behavior was not observed in the specific heat measurements. The different behavior in the field-angle dependence of H_{c2} between the electrical transport and thermodynamic measurements indicates the robust surface effect in the bulk superconductivity of CeIr₃. We have demonstrated the isotropic bulk superconductivity of CeIr₃ from thermodynamic measurements and analyzed the surface superconducting state in detail. To understand the anisotropy of the upper critical field in CeIr₃, the evaluation of surface superconductivity is important in addition to its bulk superconducting nature. The detailed investigation of H_{c2} using CeIr₃ single crystals in the present study may improve the understanding of the superconducting state in the intermediate-valence Ce compounds and the valence fluctuation mediated superconductivity.

ACKNOWLEDGMENTS

We would like to thank Y. Tokunaga, K. Izawa, S. Fujimori, A. Bhattacharyya, and D. T. Adroja for useful discussions. We acknowledge support from the International Research Center for Nuclear Materials Science (Institute for Materials Research, Tohoku University). This work was supported by KAKENHI Grants No. JP15H05884, No. JP16H04006, and No. JP19H00646, Grants-in-Aid for JSPS Research Fellows No. JP19J20539 and No. JP18F18017, and a DIARE research grant.

APPENDIX: ANGULAR DEPENDENCE OF H_{c2} OBTAINED FROM SPECIFIC HEAT MEASUREMENTS

To gain more insight into the bulk nature of the superconducting state of CeIr₃, we analyzed $H_{c2}(\theta)$ determined from specific heat measurements based on simple models. Figure 7 shows the angular dependence of H_{c2} obtained from specific heat measurements at $T = 1.85$ K. We tried to explain the angular dependence of H_{c2} based on the GL model using Eq. (4), and the fitting result is shown as a dashed blue line in Fig. 7. The fitting result is in rough agreement with the experimental $H_{c2}(\theta)$. In addition, we consider the multiband effect in the angular dependence of H_{c2} , which is determined from the specific heat measurements. We assume two simple bands, a two-dimensional Fermi surface (band1) and a three-dimensional Fermi surface (band2), as shown in the main panel of Fig. 7. These cylinder-like and three-dimensional pocket Fermi surfaces have been proposed from the band calculations in Ref. [28]. Assuming two simple bands, the angular dependence of H_{c2} in two-gap systems can be described using the following equation [37]:

$$H_{c2} = \frac{\alpha(T_c - T)}{\pi^2[\beta_1 D_1(\theta) + \beta_2 D_2(\theta)]}, \quad (\text{A1})$$

where α is a fitting parameter. β_1 and β_2 correspond to the temperature-independent band mass ratio in- and out-of-plane in the anisotropic GL equation. $D_1(\theta) = (D_1^{(a)2} \sin^2 \theta + D_1^{(a)} D_1^{(c)} \cos^2 \theta)^{1/2}$ and $D_2(\theta) = D_2^{(a)} = D_2^{(c)}$ are the angular-dependent diffusivities of band1 and band2, respectively. $D_n^{(a)}$ and $D_n^{(c)}$ ($n = 1$ and 2) are the diffusivities along the a and c axes, respectively. Assuming the anisotropic diffusivity tensor $D_1^{(a)} = 8D_1^{(c)}$ for band1, the angular dependence of H_{c2} determined from the specific heat measurements is also in

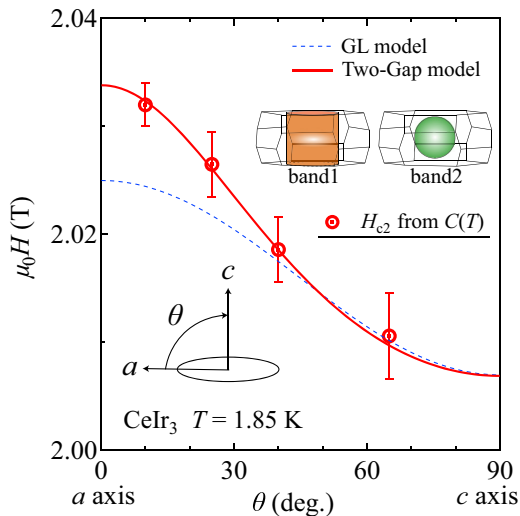


FIG. 7. Angular dependence of H_{c2} (red open circles) obtained from specific heat results measured at $T = 1.85$ K. The dashed blue line is the fitting curve of the GL model using Eq. (4). The solid red line represents the fitting result of two-gap model with angular-dependent diffusivities $D_1(\theta) = (D_1^{(a)2} \sin^2 \theta + D_1^{(a)} D_1^{(c)} \cos^2 \theta)^{1/2}$ and $D_2(\theta) = D_2^{(a)} = D_2^{(c)}$ using Eq. (A1). The schematic two-dimensional (band1) and three-dimensional Fermi surfaces (band2) are shown.

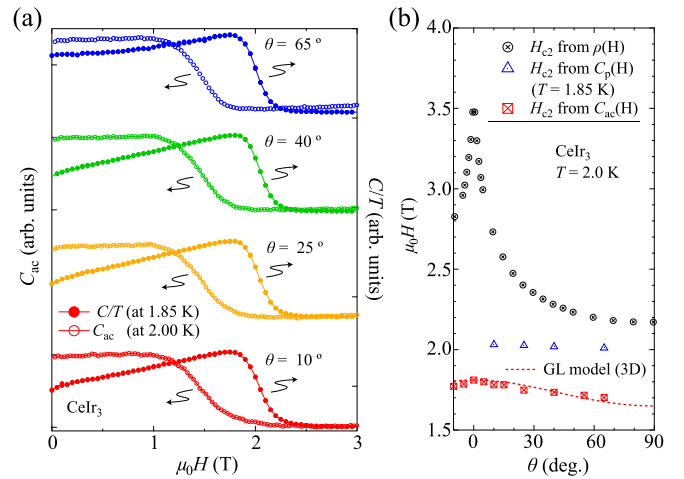


FIG. 8. (a) Field dependence of specific heat measured by means of a relaxation method and AC calorimetry in the various field angles. The measured field angles are $\theta = 10^\circ, 25^\circ, 40^\circ$, and 65° . The AC calorimetry was measured at 2 K. (b) Angular dependence of H_{c2} obtained from electrical resistivity measurements (black circles) and AC calorimetry (red squares). The dashed line is a fitting curve of GL model for H_{c2} obtained from AC calorimetry. $H_{c2}(\theta)$ obtained from specific heat measurements by means of a relaxation method at 1.85 K (blue triangles) are also shown in the same panel.

reasonable agreement with the two-gap model using Eq. (A1), as shown in Fig. 7. However, the absolute value of the difference between these two models is not very significant. More detailed experimental and theoretical studies are necessary to reveal the multiband character of the superconductivity in CeIr₃.

To obtain more information on the field-angle dependence of the upper critical field obtained from the specific heat measurements, we also performed preliminary AC calorimetry measurements using CeIr₃ single crystals at various field angles. AC calorimetry measurements were performed, using a Au/Fe-Au thermocouple as a thermometer and thin Au wires as a heater, in accordance with a method described in the Supplemental Material of Ref. [74]. Figure 8(a) shows the field dependence of specific heat measured by means of a relaxation method (C/T) and AC calorimetry (C_{ac}) at the various field angles. We detected the clear superconducting transition of CeIr₃ single crystals using AC calorimetry.

Figure 8(b) shows the angular dependence of H_{c2} obtained from the AC calorimetry at 2.0 K, with H_{c2} obtained from the specific heat measurements by means of a relaxation method at 1.85 K. Figure 8(b) also shows H_{c2} obtained from electrical resistivity at 2.0 K. The cusplike behavior was absent in $H_{c2}(\theta)$ obtained from the AC calorimetry, which is consistent with the results from the specific heat measurements using a relaxation method. The fitting result of the GL model using Eq. (4) is shown as a dashed line in Fig. 8(b). $H_{c2}(\theta)$ obtained from the AC calorimetry is also described by the GL model. Our AC calorimetry results also support the conclusion that the bulk upper critical field of CeIr₃ is rather isotropic, although CeIr₃ possesses a layered structure.

- [1] G. R. Stewart, *Rev. Mod. Phys.* **56**, 755 (1984).
- [2] M. Sigrist and K. Uuda, *Rev. Mod. Phys.* **63**, 239 (1991).
- [3] J. Flouquet, *Prog. Low Temp. Phys.* **15**, 139 (2005).
- [4] C. Pfeleiderer, *Rev. Mod. Phys.* **81**, 1551 (2009).
- [5] B. D. White, J. D. Thompson, and M. B. Maple, *Physica C* **514**, 246 (2015).
- [6] D. Aoki, K. Ishida, and J. Flouquet, *J. Phys. Soc. Jpn.* **88**, 022001 (2019).
- [7] F. Steglich, J. Aarts, C. D. Bredl, W. Lieke, D. Meschede, W. Franz, and H. Schäfer, *Phys. Rev. Lett.* **43**, 1892 (1979).
- [8] H. Q. Yuan, F. M. Grosche, M. Deppe, C. Geibel, G. Sparn, and F. Steglich, *Science* **302**, 2104 (2003).
- [9] A. T. Holmes, D. Jaccard, and K. Miyake, *Phys. Rev. B* **69**, 024508 (2004).
- [10] S. Kittaka, Y. Aoki, Y. Shimura, T. Sakakibara, S. Seiro, C. Geibel, F. Steglich, H. Ikeda, and K. Machida, *Phys. Rev. Lett.* **112**, 067002 (2014).
- [11] T. Takenaka, Y. Mizukami, J. A. Wilcox, M. Konczykowski, S. Seiro, C. Geibel, Y. Tokiwa, Y. Kasahara, C. Putzke, Y. Matsuda, A. Carrington, and T. Shibauchi, *Phys. Rev. Lett.* **119**, 077001 (2017).
- [12] J. L. Sarrao, L. A. Morales, J. D. Thompson, B. L. Scott, G. R. Stewart, F. Wastin, J. Rebizant, P. Boulet, E. Colineau, and G. H. Lander, *Nature (London)* **420**, 297 (2002).
- [13] F. Wastin, P. Boulet, J. Rebizant, E. Colineau, and G. H. Lander, *J. Phys.: Condens. Matter* **15**, S2279 (2003).
- [14] P. Monthoux, D. Pines, and G. G. Lonzarich, *Nature (London)* **450**, 1177 (2007).
- [15] K. Miyake, *J. Phys.: Condens. Matter* **19**, 125201 (2007).
- [16] A. B. Shick, J. Kolorenc, J. Ruzs, P. M. Oppeneer, A. I. Lichtenstein, M. I. Katsnelson, and R. Caciuffo, *Phys. Rev. B* **87**, 020505(R) (2013).
- [17] B. J. Ramshaw, A. Shekhter, R. D. McDonald, J. B. Betts, J. N. Mitchell, P. H. Tobash, C. H. Mielke, E. D. Bauer, and A. Migliori, *Proc. Natl. Acad. Sci. USA* **112**, 3285 (2015).
- [18] T. H. Geballe, B. T. Matthias, V. B. Compton, E. Corenzwit, F. G. W. Hull, Jr., and L. D. Longinotti, *Phys. Rev.* **137**, A119 (1965).
- [19] O. Sologub, P. Salamakha, A. P. Gonçalves, H. Ipsen, and M. Almeida, *J. Alloys Compd.* **373**, L5 (2004).
- [20] P. Hofmann, *Prog. Surf. Sci.* **81**, 191 (2006).
- [21] H. Zhang, C.-X. Liu, X.-L. Qi, X. Dai, Z. Fang, and S.-C. Zhang, *Nat. Phys.* **5**, 438 (2009).
- [22] X.-L. Qi and S.-C. Zhang, *Rev. Mod. Phys.* **83**, 1057 (2011).
- [23] Y. S. Hor, A. J. Williams, J. G. Checkelsky, P. Roushan, J. Seo, Q. Xu, H. W. Zandbergen, A. Yazdani, N. P. Ong, and R. J. Cava, *Phys. Rev. Lett.* **104**, 057001 (2010).
- [24] T. V. Bay, T. Naka, Y. K. Huang, H. Luigjes, M. S. Golden, and A. de Visser, *Phys. Rev. Lett.* **108**, 057001 (2012).
- [25] E. Parthé and R. Lemaire, *Acta Cryst. B* **31**, 1879 (1975).
- [26] Y. J. Sato, A. Nakamura, Y. Shimizu, A. Maurya, Y. Homma, D. X. Li, F. Honda, and D. Aoki, *J. Phys. Soc. Jpn.* **87**, 053704 (2018).
- [27] M. Hakimi and J. D. Huber, *Physica B+C* **135**, 434 (1985).
- [28] K. Górnicka, E. M. Carnicom, S. Gołab, M. Łapiński, B. Wiendlocha, W. Xie, D. Kaczorowski, R. J. Cava, and T. Klimczuk, *Supercond. Sci. Technol.* **32**, 025008 (2019).
- [29] N. Haldolaarachchige, L. Schoop, M. A. Khan, W. Huang, H. Ji, K. Hettiarachilage, and D. P. Young, *J. Phys.: Condens. Matter* **29**, 475602 (2017).
- [30] K. Górnicka, D. Das, S. Gutowska, B. Wiendlocha, M. J. Winarski, T. Klimczuk, and D. Kaczorowski, *Phys. Rev. B* **100**, 214514 (2019).
- [31] A. Bhattacharyya, D. T. Adroja, P. K. Biswas, Y. J. Sato, M. R. Lees, D. Aoki, and A. D. Hillier, *J. Phys.: Condens. Matter* **32**, 065602 (2019).
- [32] D. T. Adroja, A. Bhattacharyya, Y. J. Sato, M. R. Lees, P. K. Biswas, K. Panda, G. B. G. Stenning, A. D. Hillier, and D. Aoki, *arXiv:2001.03201v1*.
- [33] Y. J. Sato, Y. Shimizu, F. Honda, A. Nakamura, Y. Homma, A. Maurya, D. X. Li, and D. Aoki, *JPS Conf. Proc.* **29**, 011007 (2020).
- [34] R. C. Morris, R. V. Coleman, and R. Bhandari, *Phys. Rev. B* **5**, 895 (1972).
- [35] U. Rauchschwalbe, *Physica B+C* **147**, 1 (1987).
- [36] L. Glémot, J. P. Brison, J. Flouquet, A. I. Buzdin, I. Sheikin, D. Jaccard, C. Thessieu, and F. Thomas, *Phys. Rev. Lett.* **82**, 169 (1999).
- [37] A. Gurevich, *Phys. Rev. B* **67**, 184515 (2003).
- [38] A. Rydh, U. Welp, A. E. Koshelev, W. K. Kwok, G. W. Crabtree, R. Bruseti, L. Lyard, T. Klein, C. Marcenat, B. Kang, K. H. Kim, K. H. P. Kim, H.-S. Lee, and S.-I. Lee, *Phys. Rev. B* **70**, 132503 (2004).
- [39] F. Hunte, J. Jaroszynski, A. Gurevich, D. C. Larbalestier, R. Jin, A. S. Sefat, M. A. McGuire, B. C. Sales, D. K. Christen, and D. Mandrus, *Nature (London)* **453**, 903 (2008).
- [40] N. H. van Dijk, A. de Visser, J. J. M. France, and L. Taillefer, *J. Low Temp. Phys.* **93**, 101 (1993).
- [41] S. Kittaka, T. Nakamura, Y. Aono, S. Yonezawa, K. Ishida, and Y. Maeno, *Phys. Rev. B* **80**, 174514 (2009).
- [42] Y. Shimizu, D. Braithwaite, D. Aoki, B. Salce, and J. P. Brison, *Phys. Rev. Lett.* **122**, 067001 (2019).
- [43] D. Aoki, A. Nakamura, F. Honda, D. X. Li, Y. Homma, Y. Shimizu, Y. J. Sato, G. Knebel, J. P. Brison, A. Pourret, D. Braithwaite, G. Lapertot, Q. Niu, M. Vališka, H. Harima, and J. Flouquet, *J. Phys. Soc. Jpn.* **88**, 043702 (2019).
- [44] N. Keller, J. L. Tholence, A. Huxley, and J. Flouquet, *Phys. Rev. Lett.* **73**, 2364 (1994).
- [45] G. Rubio-Bollinger, H. Suderow, and S. Vieira, *Phys. Rev. Lett.* **86**, 5582 (2001).
- [46] H. Takahashi, K. Ishimura, T. Okamoto, E. Ohmichi, and H. Ohta, *J. Phys. Soc. Jpn.* **86**, 063002 (2017).
- [47] N. R. Werthamer, E. Helfand, and P. C. Hohenberg, *Phys. Rev.* **147**, 295 (1966).
- [48] A. Gurevich, *Physica C* **456**, 160 (2007).
- [49] L. E. DeLong, G. W. Crabtree, L. N. Hall, D. G. Hinks, W. K. Kwok, and S. K. Malik, *Phys. Rev. B* **36**, 7155 (1987).
- [50] M. Angst, S. M. Kazakov, J. Karpinski, A. Wisniewski, R. Puzniak, and M. Baran, *Phys. Rev. B* **65**, 094518 (2002).
- [51] K. Tenya, M. Ikeda, T. Tayama, T. Sakakibara, E. Yamamoto, K. Maezawa, N. Kimura, R. Settai, and Y. Ōnuki, *Phys. Rev. Lett.* **77**, 3193 (1996).
- [52] S. B. Roy, P. Chaddah, and S. Chaudhary, *Phys. Rev. B* **62**, 9191 (2000).
- [53] G. Ravikumar, V. C. Sahn, A. K. Grover, S. Ramakrishnan, P. L. Gammel, D. J. Bishop, E. Bucher, M. J. Higgins, and S. Bhattacharya, *Phys. Rev. B* **63**, 024505 (2000).
- [54] M. Marchevsky, M. J. Higgins, and S. Bhattacharya, *Nature (London)* **409**, 591 (2000).
- [55] C. P. Bean and J. D. Livingston, *Phys. Rev. Lett.* **12**, 14 (1964).

- [56] E. Zeldov, A. I. Larkin, V. B. Geshkenbein, M. Konczykowski, D. Majer, B. Khaykovich, V. M. Vinokur, and H. Shtrikman, *Phys. Rev. Lett.* **73**, 1428 (1994).
- [57] J. M. Lu, O. Zheliuk, I. Leermakers, N. F. Q. Yuan, U. Zeitler, K. T. Law, and J. T. Ye, *Science* **350**, 1353 (2015).
- [58] I. Banerjee, Q. S. Yang, C. M. Falco, and I. K. Schuller, *Phys. Rev. B* **28**, 5037 (1983).
- [59] M. Tinkham, *Phys. Rev.* **129**, 2413 (1963).
- [60] D. Saint-James and P. G. de Gennes, *Phys. Lett.* **7**, 306 (1963).
- [61] K. Yamafuji, E. Kusayanagi, and F. Irie, *Phys. Lett.* **21**, 11 (1966).
- [62] G. Deutscher, *J. Phys. Chem. Solids* **28**, 741 (1967).
- [63] M. Shimozawa, S. K. Goh, T. Shibauchi, and Y. Matsuda, *Rep. Prog. Phys.* **79**, 074503 (2016).
- [64] C.-R. Hu and V. Korenman, *Phys. Rev.* **178**, 684 (1996).
- [65] C.-R. Hu and V. Korenman, *Phys. Rev.* **185**, 672 (1996).
- [66] N. Keller, J. L. Tholence, A. Huxley, and J. Flouquet, *Phys. Rev. B* **54**, 13188 (1996).
- [67] C. C. Chin and T. P. Orlando, *Phys. Rev. B* **37**, 5811 (1988).
- [68] S. Yonezawa, *Condens. Matter* **4**, 2 (2019).
- [69] M. P. Smylie, K. Willa, H. Claus, A. E. Koshelev, K. W. Song, W.-K. Kwok, Z. Islam, G. D. Gu, J. A. Schneeloch, R. D. Zhong, and U. Welp, *Sci. Rep.* **8**, 7666 (2018).
- [70] J. W. Allen, S. J. Oh, M. B. Maple, and M. S. Torikachvili, *Phys. Rev. B* **28**, 5347 (1983).
- [71] H. Sugawara, T. Yamazaki, J. Itoh, M. Takashita, T. Ebihara, N. Kimura, P. Svoboda, R. Settai, Y. Ōnuki, H. Hideyuki, S. Uji, and H. Aoki, *J. Phys. Soc. Jpn.* **63**, 1502 (1994).
- [72] B. T. Matthias, T. H. Geballe, and V. B. Compton, *Rev. Mod. Phys.* **35**, 1 (1963).
- [73] H. Okamoto, *J. Phase Equilib.* **12**, 563 (1991).
- [74] D. Aoki, F. Honda, G. Knebel, D. Braithwaite, A. Nakamura, D. X. Li, Y. Homma, Y. Shimizu, Y. J. Sato, J.-P. Brison, and J. Flouquet, *J. Phys. Soc. Jpn.* **89**, 053705 (2020).